NSRRC - Jo 4162 (2015)

Macromolecules

Article

pubs.acs.org/Macromolecules

Large-Area Block Copolymer Photonic Gel Films with Solvent-Evaporation-Induced Red- and Blue-Shift Reflective Bands

Yeo-Wan Chiang,*[,†] Chung-Yi Chou,[†] Cheng-Sian Wu,[†] En-Li Lin,[†] Jongseung Yoon,[‡] and Edwin L. Thomas*[,§]

[†]Department of Materials and Optoelectronic Science, Center for Nanoscience and Nanotechnology, National Sun Yat-Sen University, Kaohsiung 80424, Taiwan

[‡]Department of Materials Science, University of Southern California, Los Angeles, California 90007, United States

[§]Department of Materials Science and NanoEngineering, Rice University, Houston, Texas 77005, United States

Supporting Information

ABSTRACT: By choice of large overall molecular weights from 0.5 to 1 M kg/mol, the lamellar microstructures of the high-molecular-weight polystyrene-*block*-polyisoprene (PS–PI) block copolymers (BCPs) exhibited various long periods and associated different reflected wavelengths. Interestingly, unique solvatochromism-dependent red- and blue-shift reflective bands could be acquired in the PS–PI BCP gel films using a nonselective neutral solvent as an external stimulus. At low polymer concentration, red-shift of the reflectivity was attributed to the increase of BCP long period by the enhancement of the BCP segregation strength, namely, a thermodynamically controlled swelling process. In contrast, at high polymer concentration (ϕ_p > 0.8), the blue-shifting reflectivity resulted from the decrease of the BCP long period by the collapse of polymer chains, namely, a kinetically controlled deswelling process. Also, well-aligned lamellar microstructures were fabricated using a shear-induced microstructural orientation. This provides a simple way to fabricate large-area 1D photonic gel films with uniform reflective colors.

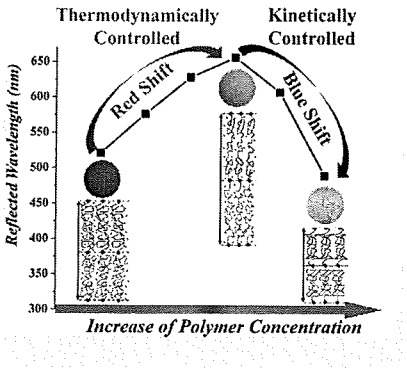

INTRODUCTION

Periodic ordered nanostructures created from bottom up (i.e., self-assembly) approaches are well-known in providing fast and economy processes, functionalized and biocompatible advantages in various application fields.[1] Regarding self-assembly from block copolymers (BCPs), the microphase-separation can be accomplished by the immiscibility from the chemical differences between the constituent blocks.[2] Owing to the various possible ordered microstructures, BCP self-assembly may provide diverse applications for nanotechnological applications and has been intensively investigated.[3−5] Self-assembled BCPs having high molecular weights (M_w) are promising to fabricate organic photonic crystals due to the ordered microphase-separated structures and the appropriate domain spacing with respect to the wavelength of visible light. The optical properties of the photonic crystals are strongly dependent on the lattice structure, domain spacing, dielectric contrast and lattice orientation.[6] By taking advantage of BCP characteristics, manipulation of the photonic properties becomes promising. Accordingly, a variety of the microphase-separated morphologies from the self-assembly of the high-M_w BCPs such as one-dimensional (1-D) lamellae, 2-D hexagonally packed cylinders, and 3-D double gyroid structures are able to give different kinds of photonic crystals with various reflective bandgaps at visible and near-IR frequencies.[7−17] By introducing inorganic materials into the BCP-based photonic crystals through hybridization, the control and enhancement of the photonic properties can be carried out.[18] Also, self-assembled BCP photonic crystals are highly responsive to different kinds of external stimuli such as solvent, temperature and compressive mechanical strain so the shift of wavelength of the bandgap can act as a sensing mechanism.[18−27]

In this study, the fabrication of organic BCP photonic gel films from the self-assembly of high-M_w polystyrene-*block*-polyisoprene (PS–PI) BCPs having three different molecular weights was conducted. The wavelength-shift of the reflectivity bands was strongly dependent on the polymer concentration, first revealing a red-shift and subsequently a blue-shift in the reflective bands with the increase of polymer concentration as the toluene evaporated from the PS–PI gel films. This variation in lamellar period was due to interplay between the thermodynamically controlled BCP segregation strength and the kinetics of solvent evaporation. Large-area BCP photonic crystals with uniform thickness and reflective colors could be fabricated using oscillatory shear. Design of stimuli-responsive BCP photonic crystals is also discussed.

Received: April 10, 2015
Revised: May 19, 2015
Published: June 2, 2015

ACS Publications © 2015 American Chemical Society

DOI: 10.1021/acs.macromol.5b00744
Macromolecules 2015, 48, 4004−4011

Table 1. Characteristics of High-M_w PS–PI Block Copolymers

sample	$M_{w,PS}$[a] (kg/mol)	$M_{w,PI}$[b] (kg/mol)	total M_w[c] (kg/mol)	f_{PS}[a]	PDI[d]	D_L[e] (nm)	d_{PS}[f] (nm)	d_{PI}[f] (nm)
PS/PI-260/278	260	278	538	0.45	1.02	118	49.4	68.6
PS/PI-340/363	340	363	703	0.45	1.02	147	59.9	87.1
PS/PI-505/520	505	520	1025	0.46	1.02	164	66.3	97.7

[a]Determined by GPC. [b]Obtained from ^{1}H NMR measurement. [c]Obtained from 1 plus 2. [d]Determined by GPC. [e]Calculated by USAXS. [f]Calculated by 1-D correlation function.

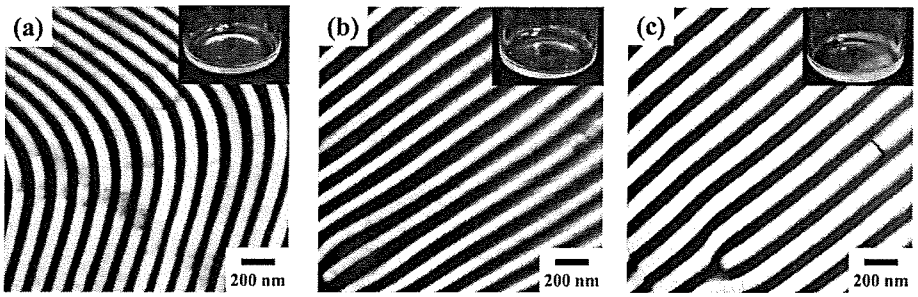

Figure 1. TEM micrographs of the photonic PS–PI BCPs. (a) PS/PI-260/278, (b) PS/PI-340/363, and (c) PS/PI-505/520 BCPs. After OsO_4 staining, the PI microdomains are dark and the PS microdomains are bright. The insets show the optical photographs of the high-M_w PS–PI BCP gels in toluene.

EXPERIMENTAL SECTION

Materials. A series of high-M_w PS–PI BCPs were anionically synthesized via sequential addition of styrene and isoprene monomers into cyclohexane/benzene mixed solvent. The molecular weights and compositions of the PS–PI BCPs were determined by gel permeation chromatography (GPC) and nuclear magnetic resonance (NMR). On the basis of molecular weight and volume fraction, the PS–PI BCPs are assigned as PSx-PIy in which x and y represent the molecular weights (kg/mol) of PS and PI blocks, respectively. The volume fractions of the PS block are estimated by assuming that the densities of PS and PI are 1.05 and 0.905 g/cm^3, respectively (see Table 1).

Sample Preparation. Bulk samples (0.5 mm thick ×30 mm diameters) of the PS–PI block copolymers were prepared by solution casting onto glass substrates from toluene solution (5 wt %) at room temperature over 2 weeks. The thickness of the dried bulk film is around 0.5 mm. The bulk samples were then dried in a vacuum oven at 100 °C for 3 days to remove any residual solvent.

Shear-Induced Orientation. To prepare well-oriented lamellar microstructures of the high-M_W BCP gels, oscillatory shearing was conducted. The PS–PI BCP was dissolved in toluene (8–14 wt %) and was placed on a glass slide and then subsequently covered with another glass slide on the top to form a sandwich structure. We conducted the shear alignment by oscillatory rotation along tangent direction by hand. After shearing, the optical properties of the BCP photonic gels were then examined using a spectrometer microscope equipped with an optical spectrometer.

Transmission Electron Microscopy (TEM). A series of as-cast bulk samples and the shear-oriented films were cryo-microtomed at −120 °C for transmission electron microscope (TEM) observation. A Reichert Ulracut microtome equipped with a Reichert FCS cyrochamber and a diamond knife was utilized. Staining was accomplished by exposing the microsections to the vapor of a 4 wt % aqueous OsO_4 solution for 30 min. Bright field TEM images employing mass–thickness contrast were obtained from the stained microsections on a JEOL JEM-2100 TEM, at an accelerating voltage of 200 kV. After staining by OsO_4 vapor, PS microdomains appear bright and the PI microdomains appear dark due to the enhanced difference of the mass–thickness contrast by preferential OsO_4 staining the unsaturated rubber blocks.

X-ray Experiments. Ultra-small-angle X-ray scattering (USAXS) experiments were conducted at the synchrotron X-ray beamline 23A1 at the National Synchrotron Research Center (NSRRC) in Taiwan. The wavelength of the X-ray beam was 0.2066 nm and the distance for the sample to detector was 5075.2 mm. A MAR CCD X-ray detector (MAR USA) was used to collect the two-dimensional (2-D) SAXS patterns. One-dimensional (1-D) SAXS profiles were obtained by azimuthal integration of the 2-D SAXS patterns. The scattering angle of the SAXS pattern was calibrated using silver behenate, with the first-order scattering vector of silver behenate q^* ($q^* = 4\pi\lambda^{-1} \sin\theta$, where 2θ is the scattering angle) equal to 1.076 nm^{-1}.

Reflectivity Measurements. Reflectivity spectra for as-cast samples were examined using an optical microscope (ESPA N-800M) equipped with a fiber-optic spectrometer (B&W Tek i-trometer). An Ag mirror is used as 100% reflectivity standard. Because of the effect of the numerical aperture of the objective lens (10×, N.A. $= n_{air} \sin\theta = 0.3$), the reflectivity spectrum is a convolution of reflectivity spectra measured over an incident angle of 0–17.5°.

Normalized 1-D Correlation Function. To resolve the thicknesses of the PS (d_{PS}) and PI (d_{PI}) microdomains, we applied the normalized 1D correlation function to the USAXS data. The normalized 1D correlation function [$\gamma(z)$] can be obtained using the equation[28]

$$\gamma(z) = \frac{1}{Q}\int_0^\infty q^2 I(q)\cos(qz)\,dq$$

where z is the coordinate along the electron density distribution; q is the scattering vector; $I(q)$ is the observed 1D intensity; and the invariant Q is the integrated scattering intensity with respect to q, defined by

$$Q = \int_0^\infty q^2 I(q)\,dq$$

First, thermal fluctuations were subtracted from the observed scattering intensity by evaluating the slopes of plots of $I(q)q^4$ versus q^4 at wide scattering vectors q, so as to fit the 1D correlation function. Accordingly, the correlation function [$\gamma(z)$] varied with respect to the real space coordinate (z) was plotted using the normalized 1D correlation function. The characteristic spacing for the thinner layer (i.e., d_{PS}) from the intercept (for the real space coordinate axis) was calculated from the tangent line near the position at $z = 0$.

RESULTS AND DISCUSSION

Microdomain Structures of High-M_w PS–PI Block Copolymers. Microphase-separated morphologies of the as-

DOI: 10.1021/acs.macromol.5b00744
Macromolecules 2015, 48, 4004–4011

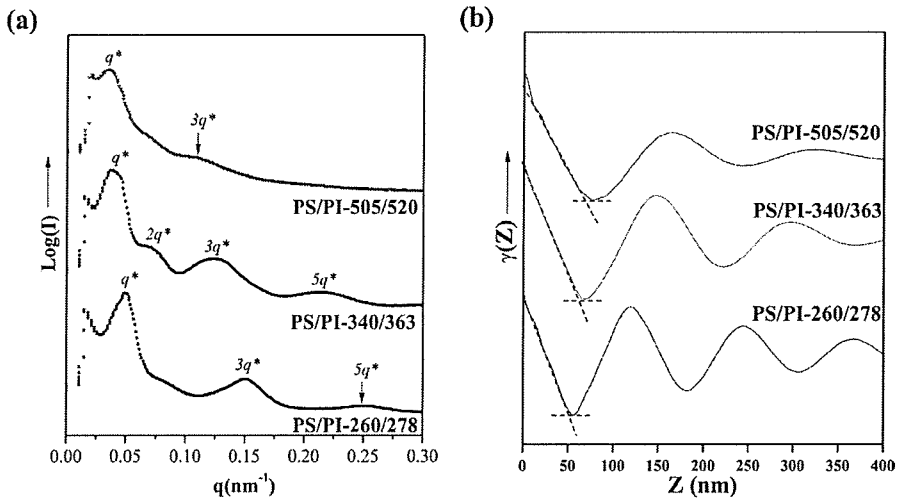

Figure 2. (a) 1-D USAXS profiles and (b) normalized 1-D correlation function of the neat PS/PI-260/278, PS/PI-340/363, and PS/PI-505/520 BCPs after solution casting from toluene. The (001) peaks correspond to 118, 147, and 164 nm for PS/PI-260/278, PS/PI-340/363, and PS/PI-505/520 BCPs, respectively.

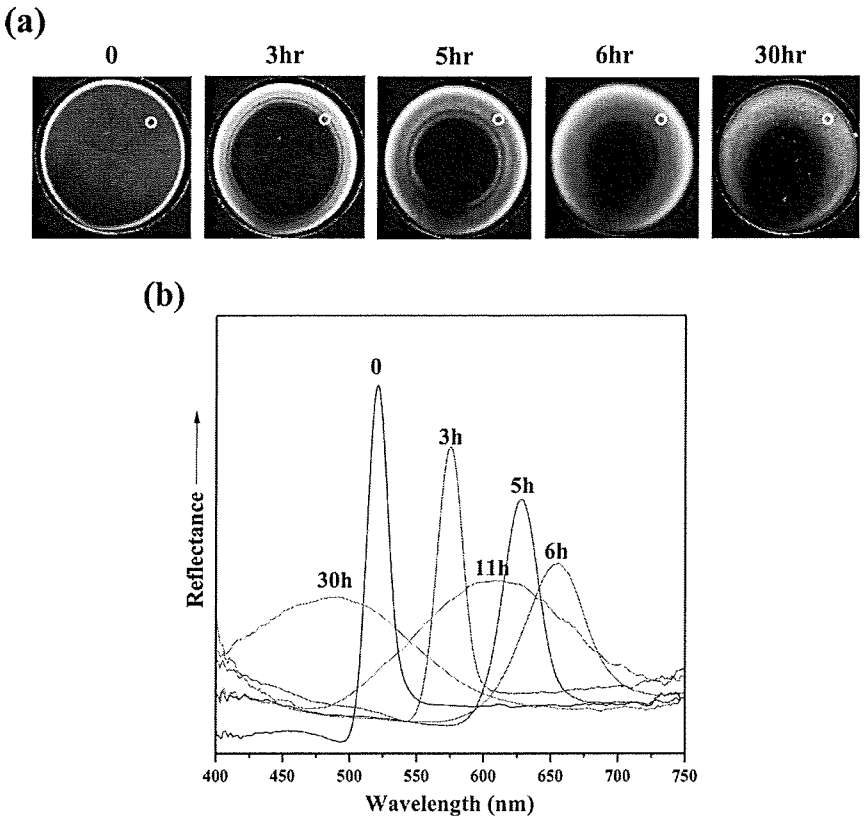

Figure 3. (a) Time-dependent color change for the PS/PI-505/520 photonic gel films during solvent evaporation. (b) Corresponding time-dependent reflectivity spectra taken at the white circle position in the PS/PI-505/520 photonic gel. The initial intense blue color at the white circle position exhibits green, red, and then red-orange before shifting and broadening to green and white-blue colors.

cast high-M_w PS–PI BCPs having various molecular weights were then examined by TEM and USAXS. The TEM micrographs show well-ordered lamellar microstructures in the PS/PI-260/278, PS/PI-340/363, and PS/PI-505/520 BCPs (Figure 1). The 1-D USAXS profiles show reflections at relative q^* ratios of 1:2:3, confirming the formation of the expected lamellar microstructures in the as-cast high-M_w PS–PI BCPs (Figure 2a). Also, a progressive shift of the first reflection peak to lower q indicates the expected increase of the BCP long period with the increase of the BCP overall molecular weight.

DOI: 10.1021/acs.macromol.5b00744
Macromolecules 2015, 48, 4004–4011

The calculated long periods (D_L) of the PS/PI-260/278, PS/PI-340/363, and PS/PI-505/520 BCPs are 118, 147, and 164 nm, respectively. Using the 1-D correlation function approach (Figure 2b), the respective microdomain spacings can be estimated (Table 1).

The spectral position of the reflectivity peak from a 1-D photonic crystal is strongly dependent upon the microstructural spacing. Accordingly, as the long period of the BCP lamellar microstructures becomes larger, the wavelength of the characteristic reflective electromagnetic waves also increases due to the increase of the optical thickness.[6] During solution casting, the initially clear PS–PI solution (i.e., a homogeneous disordered phase) transforms into the colorful PS–PI gel phase (see insets in Figure 1). The appearance of color is concentration-dependent and is also dependent on the overall M_w of the PS–PI BCP. This behavior is attributed to the decrease of the order–disorder transition concentration (ϕ_{ODC}) with the increased M_w of the PS–PI BCP. According to the solubility parameters of PS ($9.1(cal/cm^3)^{1/2}$), PI ($8.2(cal/cm^3)^{1/2}$) and toluene ($8.8(cal/cm^3)^{1/2}$), toluene can be regarded as a good, approximately neutral solvent for both PS and PI. We found that the ϕ_{ODC} are 13.5, 9.3, and 7.5 wt % for the PS/PI-260/278, PS/PI-340/363, and PS/PI-505/520 BCPs, respectively.

Red- and Blue-Shift Reflectance of the Photonic Bandgaps in Sequence. It is interesting to investigate the interaction between the solvent molecules and BCP microdomains associated with the variation of the reflective bands in the self-assembly of BCP photonic crystals. The PS/PI-505/520 BCP was first dissolved in toluene (5 wt %). At 9 wt %, the gel-like PS/PI-505/520 solution was cast between two glass substrates to form the photonic gel film. Figure 3a shows time-dependent photographs of the PS/PI-505/520 BCP photonic gel film. Obviously, the wavelength of the reflective color depends on the polymer concentration over time. As the polymer concentration reaches ϕ_{ODC}, the swollen lamellar microdomains forms, resulting in the reflectance of visible wavelength at $t = 0$. With elapse of time, the variation of the reflective colors is strongly dependent on the radial position due to the distribution of the solvent concentration resulted from the solvent evaporation at the rim edge.[17] The corresponding reflectivity spectra were examined at a fixed radial position (i.e., white circle in Figure 3a) as a function of time. The peak reflectivity occurs at 520 nm for an initial measurement at $t = 0$. With elapse of time, the evaporation of the solvent first caused the reflective band to red shift to the longer wavelength region as $t = 3–5$ h. At $t = 6$ h, the peak position of the reflective band reaches a maximum value at 655 nm. Interestingly, instead of further continuous red shifting, the reflective band now exhibits a blue shift (606 nm) at $t = 11$ h. Finally, as $t \geq 30$ h, the band is very broad centered at 498 nm and exhibits no further change with time. As a result, the strong, narrow reflectivity peaks were obtained initially and broadness of the peaks was observed with loss of solvent. The peak wavelength of reflective light for a multilayer stack of the PS–PI BCP is expressed as eq 1.

$$\lambda_{peak} = 2[n_{PS}d_{PS} + n_{PI}d_{PI}] \quad (1)$$

where λ_{peak} is the first–order peak wavelength at normal incidence; n_{PS} and n_{PI} are the refractive indices for the PS and PI components (for the dry film, n_{PS} =1.59 ; n_{PI} =1.51), respectively; d_{PS} and d_{PI} are the respective thicknesses for the PS and PI microdomains and can be determined by the normalized 1-D correlation function (Table 1). As calculated, λ_{peak} is 506 nm for the PS/PI-505/520 BCP at a dried state, which is similar to that at $t \geq 30$h (498 nm), suggesting the complete evaporation of toluene after 30h.

We suggest that the occurrence of the first red- and then blue-shift reflective bands in sequence with the decrease of the solvent concentration is the consequence of the variation of the BCP lamellar long period resulting from the competition between the swelling due to increased segregation strength and the contraction due to solvent evaporation for the BCP long period. With the decrease of the solvent concentration, the reflective band exhibits the progressive decrease of the reflectivity intensity with an accompanying increase of the reflectivity bandwidth (the full width at the half-maximum, fwhm). The evaporation of the toluene solvent from the rim edge drives the outward diffusion of the PS–PI BCP along radial direction to fill the empty space resulting from the reduced solvent volume in the PS–PI gel film. This may result in the nonuniform thickness of the PS–PI gel film evidenced by the absence of the reflectance in the center of the photonic gel film as t=5h (Figure 3a). Meanwhile, the fast evaporation of the toluene ($V_{toluene}$ = 24.8 mmHg at 25 °C) may give rise to stress on the PS–PI layers, resulting in the disorientation of the originally high parallel lamellar microstructures. After the removal of the glass substrates in liquid nitrogen, the cross-sectional morphology was then examined by TEM. As shown in Figure 4, disoriented lamellar microstructures are observed,

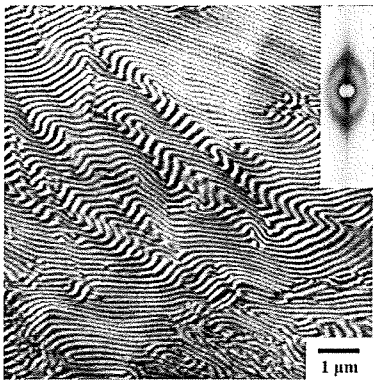

Figure 4. Cross-sectional TEM micrograph of the as-cast PS/PI-505/520 film after the complete evaporation of the solvents. The inset shows the corresponding 2-D USAXS pattern.

which is consistent with the corresponding isotropic ring-like texture of the 2-D USAXS pattern (the inset in Figure 4). Consequently, the decrease of the reflected intensity and broadening of the reflectivity band due to layer tilt is obtained. The fwhm of the reflective bands increases strongly from 19 nm ($t = 0$) to 155 nm ($t = 30$ h), due to the variation of the effective refractive index contrast and layer tilt during solvent evaporation. Figure S1 (Supporting Information) shows the effective refractive index, n_{eff}, of the PS and PI layers varies with the neutral solvent composition by using eq 2.

$$n_{eff} = n_p\phi_p + n_s(1 - \phi_p) \quad (2)$$

where n_{eff} is the effective refractive index of a microdomin containing solvent, n_p is the refractive index of the particular block, n_s is the refractive index of a solvent and ϕ_p is the volume fraction of the polymer in a layer. The refractive indices (at λ =

DOI: 10.1021/acs.macromol.5b00744
Macromolecules 2015, 48, 4004–4011

600 nm) of the PS, PI and toluene are 1.59, 1.51, and 1.50, respectively. Obviously the effective refractive index contrast $[\Delta n_{eff} = \phi_p(n_{PS} - n_{PI})]$ increases with the decrease of the solvent composition. Consequently, the broadening of the reflectivity peak results from the enhancement of the effective refractive index contrast and the layer tilt with the decrease of the solvent concentration. This is consistent with the simulated reflectivity spectra as the value of n_H/n_L increases.[6]

The microdomain size of BCPs varied with temperature, polymer concentration and molecular weight has been demonstrated.[29−37] In the solvatochromic process, the peak position of the reflectivity band at low polymer concentration can be expressed as eq 3.[17]

$$\lambda_{peak} = 2n_{eff}L \cong 2\alpha n_{eff}\phi_p^{1/6} \quad (3)$$

where n_{eff} is the solvent-dependent average index of reflection of the dielectric stack, L is the long period of the lamellar BCP and α is a proportionality constant. At high polymer concentration, long period can be determined as eq 4 in accordance with $L \propto \phi_p^{-1}$ as suggested by Hashimoto and co-workers.[30,31]

$$\lambda_{peak} = 2n_{eff}L \cong 2\beta n_{eff}\phi_p^{-1} \quad (4)$$

where β is a proportionality constant. If we assume a neutral solvent, then the film at all of the swollen states has the same layer thickness ratio (d_{PS}/d_{PI}) which is the same as the dried state. This yield the n_{eff} of the swollen lamellar stacking as

$$n_{eff} = 0.4[\phi_p n_{PS} + (1 - \phi_p)n_{toluene}] + 0.6[\phi_p n_{PI} + (1 - \phi_p)n_{toluene}] \quad (5)$$

We assume that the polymer concentration at $t = 0$ is the same as the initially prepared polymer concentration in toluene (ϕ_p = 9 wt % = 0.09 (w/w)). Then the proportionality constant α = 259 nm can be calculated. Also, as the film is completely dried ($\phi_p = 1$) at t = 30 h, β = 161 nm can also be determined. Accordingly, the material parameters including the solvated long period D_L and n_{eff} can be calculated in Table 2. Notably,

Table 2. Material Parameters of the PS/PI-505/520 BCP in the Solvatochromic Process

t (h)	λ_{peak} (nm)	D_L (nm)	ϕ_p (w/w)	n_{eff}	d_{PS} (nm)	d_{PI} (nm)
0	521	173	0.09	1.504	69.3	103.7
3	576	191	0.161	1.507	76.4	114.6
5	628	208	0.267	1.511	83.2	124.8
6	655	216	0.340	1.514	86.4	129.6
		214	0.753	1.532	85.6	128.4
11	609	199	0.811	1.534	79.6	119.4
30	498	161	1.0	1.542	64.4	96.6

the parameters at the longest reflective band of 655 nm can be either calculated by eqs 3 or 4, such that two sets of the data are presented. As λ_{peak} = 655 nm, the almost identical D_L from eq 3 and 4 indicates a dynamic equilibrium of swelling and deswelling effects at ϕ_p = 0.340−0.753 in the solvatochromic process.

In a block copolymer solution with a nonselective (neutral) solvent, the variation of the BCP lamellar long period with the increase of the polymer concentration (or the decrease of the solvent concentration) is mainly dominated by the competition between the thermodynamically controlled swelling effect by BCP segregation strength and kinetically controlled deswelling effect by solvent evaporation.[30,31] Figure 5 displays the proposed mechanism for the solvatochromism-dependence of the initial red-shift and then the subsequent blue-shift with polymer concentration. In Figure 5a, when the polymer concentration is lower than the ϕ_{ODC}, i.e., $\phi_{p0} < \phi_{ODC}$, the BCP solution having large amounts of solvent is a like low-viscosity homogeneous mixture (Figure 5a). As the solvent evaporates over time and the polymer concentration reaches the ϕ_{ODC} (i.e., $\phi_{p1} = \phi_{ODC}$), the BCP solution becomes a gel state having an ordered microphase-separated swollen lamellar phase due to the unchanged symmetric composition in a neutral solvent (Figure 5b). With the continued decrease of solvent concentration ($\phi_{p2} > \phi_{ODC}$), the shrinkage of the average distance between A-B junctions (i.e., $a_{j2} < a_{j1}$) and the enhancement of the BCP segregation strength give rise to the stretching of the PS and PI block chains along the lamellar normal, namely, swelling effect. As reported,[34] the D_L is proportional to $\phi_p^{1/6}$ at low polymer concentration. Therefore, the increase of D_{L1} to D_{L2} results in the red shift of the reflectivity band as $\phi_{p2} > \phi_{ODC}$ (Figures 5b and 5c). Accordingly, a maximum in the BCP long period can be obtained with the continuingly intensified BCP segregation strength, reaching the longest reflectivity wavelength of 655 nm as t = 6 h (Figure 3b). Consequently, at low polymer concentration, i.e., $\phi_p > \phi_{ODC}$, the red shifting of the reflective bands is mainly determined by the thermodynamically controlled swelling of the BCP long period.

However, at high polymer concentration, i.e., $\phi_{ODC} \ll \phi_{p3} \leq 1$, the glass transition temperature of the PS block reaches ambient temperature and the viscosity of the PS−PI BCP gel is increased such that the molecular rearrangements associated with the displacement of the A-B junctions along the interface are dramatically slowed down, namely, virtually frozen a_{j2}. Meanwhile, to maintain a uniform density distribution in the microdomains, the block chains must contract with the continued evaporation of the solvent, i.e., deswelling effect. As a result, the decrease of D_L accompanying with the blue-shift reflective bands can be observed as $\phi_{ODC} \ll \phi_{p3} \leq 1$, namely, the kinetically controlled deswelling process (Figures 5c and 5d). Here the D_L is proportional to ϕ_p^{-1} for anisotropic lamellar microdomains at high polymer concentration. In contrast to the reflectance change of the cumene-solvated PS−PI gel film,[17] owing to the solidification of the PS−PI BCP at the rim edge resulted from the very low evaporation rate of the cumene (V_{cumene} = 4.5 mmHg at 25 °C), the cumene solvent was largely trapped inside the gel film (i.e., at low polymer concentration) such that the blue-shift phenomenon is thus absent.

Large-Area Block Copolymer Photonic Crystals by Shear-Induced Orientation. Except for the gradient distribution of the solvent concentration, the nonuniform reflective colors at the rim edge and at the center in the toluene-solvated PS−PI gel film might be attributed to the disorientation of the lamellar microstructures and nonuniform thickness due to the fast evaporation of toluene (Figure 3a). Although the utilization of the slow-evaporated cumene can drive the formation of well-oriented lamellar microstructures in the cumene-solvated PS−PI gel film,[17] the BCP photonic film evaporated from the low-polymer-concentration solution always exhibits nonuniform thickness due to the huge loss of the solvent. For practical applications, a well-aligned BCP photonic film with uniform thickness in a dried state is critical and

DOI: 10.1021/acs.macromol.5b00744
Macromolecules 2015, 48, 4004−4011

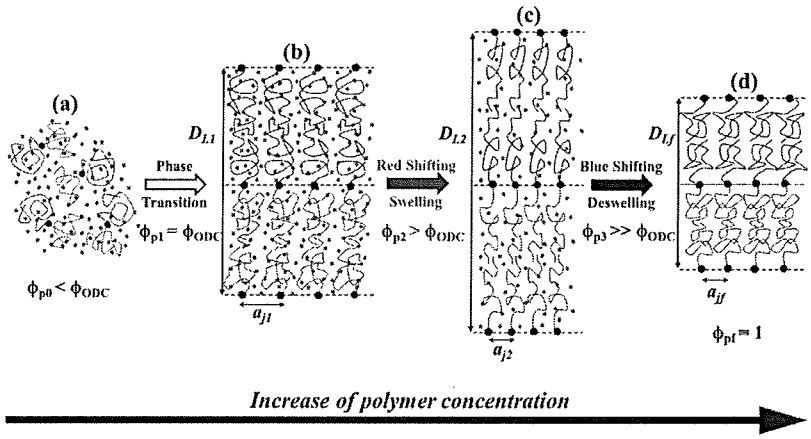

Figure 5. Proposed mechanism for the initial red-shift and then subsequent blue-shift reflectivity with the increase of the polymer concentration ϕ_p. The small spheres, D_L, a_j represent as neutral solvent molecules, BCP long period and average junction distance, respectively.

necessary. Here a facile process was developed to generate large-area 1-D BCP photonic crystals with uniform thickness using oscillatory shear. As shown in Figure 6, the shear-aligned

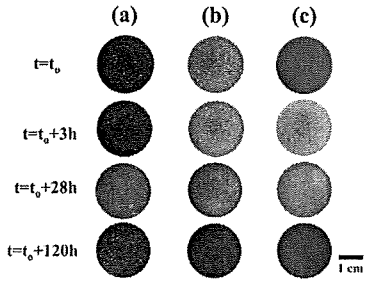

Figure 6. Time-dependent optical photographs for the shear-aligned (a) PS/PI-260/278, (b) PS/PI-340/363, and (c) PS/PI-505/520 BCP photonic gel films. Here t_0 means the time starting to measure the reflectance after shearing.

PS/PI-260/278, PS/PI-340/363 and PS/PI-505/520 BCP photonic gel films all exhibit uniform reflective colors over the entire area as $t = t_0$. Because the solvent continuously evaporates during shearing, the concentration gradient in the shear-aligned BCP gel becomes more insignificant than that in the as-cast BCP gel. Accordingly, the reflective bands are almost independent of the radial direction in these shear-aligned BCP gels. Different from the absent reflectance at the center of the PS–PI gel film (≥5 h) in Figure 3, the shear-aligned PS–PI gel films all possess significant reflectance for the entire area. This is attributed to the uniform thickness of the PS–PI gel film driven by shear field. We also found that depending on the shear amplitude and frequency, the smaller strain and lower frequency could give better uniform reflective color, consisting to the long relaxation time of the high-M_w BCP chains.[38]

Figure 7 shows the corresponding time-dependent reflectivity spectra of the shear-aligned PS–PI photonic gel films. Similarly, the red-shift reflective bands are first obtained and blue-shift reflective bands are subsequently found with elapse of time in the sheared-aligned PS/PI-260/278 and PS/PI-340/363 photonic gel films (Figure 7, parts a and b). Notably, only blue shift of the reflectivity bands can be observed in the shear-aligned PS/PI-505/520 photonic gel films (Figure 7c). In contrast to PS/PI-260/278 and PS/PI-340/363 BCPs, it requires much more time (i.e., longer t_0) to accomplish well-aligned parallel lamellar microstructures for the highest-M_w PS/PI-505/520 BCP. Accordingly, the large evaporation of the solvent during shearing resulted in the absence of the red-shift reflectance at the low polymer concentration in the following reflectance measurement. The M_w effect on the reflected wavelength is significant through the observation of the reflective colors for the PS–PI BCP gels. With the increase of the M_w, the longer-wavelength reflective bands can be found. As observed, the maximum positions of the reflective bands for the shear-aligned PS/PI-505/520, PS/PI-340/363, and PS/PI-260/278 are 666, 509, and 460 nm, respectively. Interestingly, these PS–PI BCP films can still exhibit uniform reflective colors for the entire area even though time is extremely long ($t = t_0 + 120$ h), suggesting that the well-aligned lamellar microstructures are preserved after solvent evaporation. This can be confirmed by the cross-sectional TEM micrograph for the shear-aligned PS/PI-340/363 BCP gels after the complete evaporation of toluene in Figure 8. As shown, the long-range and well-aligned lamellar microstructures oriented parallel to shear direction are observed, which are consistent with the 2-D USAXS pattern having intense anisotropic reflections along meridian direction (the inset in Figure 8). As a result, the large-area PS–PI BCP photonic crystals can be successfully carried out using oscillatory shear stress.

CONCLUSIONS

The solvent-responsive BCP photonic crystals can be fabricated from high-M_w and lamella-forming PS–PI BCPs using toluene as the external stimulus. The unique solvatochromism-dependent red- and blue-shift reflectivity bands varied with polymer concentration can be observed. In the low-concentration regime ($\phi_{ODC} < \phi_p$), the red-shift reflectivity band is due to the thermodynamically controlled swelling of BCP long period by the intensified BCP segregation strength. By contrast, in the high-concentration regime ($\phi_{ODC} \ll \phi_p \leq 1$), the blue-shift reflectivity band is attributed to the kinetically controlled deswelling of the BCP long period by the collapse of the block chains. Using oscillatory shear stress, large-area and highly aligned 1-D photonic crystals with uniform thickness and reflectivity can be carried out. The highly aligned lamellar microstructures can be still preserved after the complete

DOI: 10.1021/acs.macromol.5b00744
Macromolecules 2015, 48, 4004–4011

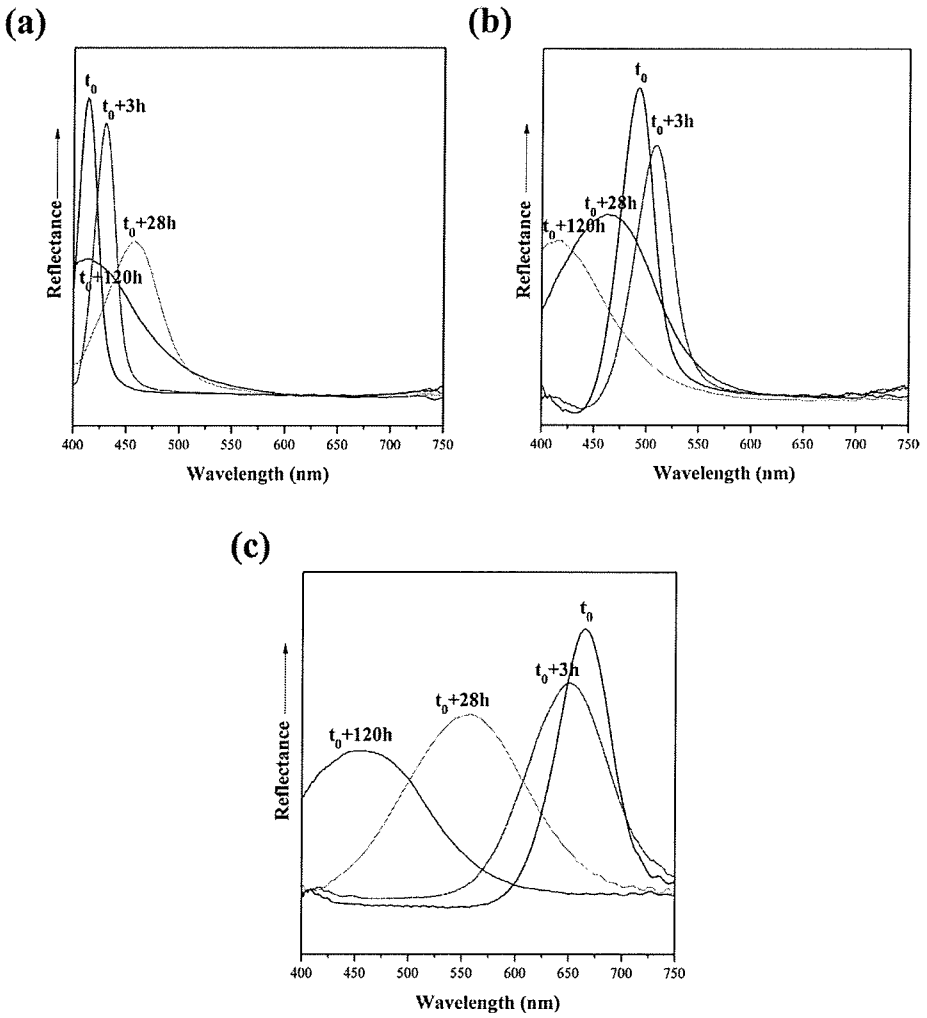

Figure 7. Corresponding reflectivity profiles as a function of time for the shear-aligned (a) PS/PI-260/278, (b) PS/PI-340/363, and (c) PS/PI-505/520 BCP photonic gels. The color of the film initially red shifts and then blue shifts as the solvent evaporates. Here $t = 0$ means the time starting to measure the reflectance after shearing.

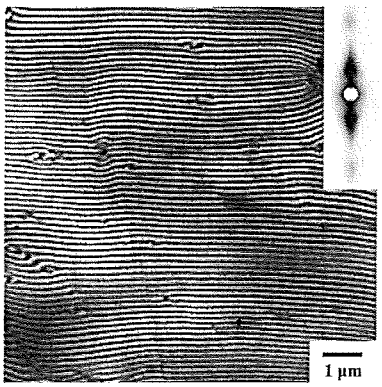

Figure 8. Cross-sectional TEM micrograph of the shear-aligned PS/PI-340/363 film after complete solvent evaporation. The inset shows the corresponding 2-D USAXS pattern.

evaporation of the solvent. This may provide a novel concept for designing tunable stimuli-responsive BCP photonic reflectors through the thermodynamically or kinetically controlled process.

■ ASSOCIATED CONTENT

Supporting Information

Effective refractive index of the PS and PI varying with solvent composition. The Supporting Information is available free of charge on the ACS Publications website at DOI: 10.1021/acs.macromol.5b00744.

■ AUTHOR INFORMATION

Corresponding Authors

*(Y.-W.C.) Telephone: +886-7-5252000. Fax: +886-5-5254099. E-mail: ywchiang@mail.nsysu.edu.tw.
*(E.L.T.) E-mail: elt@rice.edu.

DOI: 10.1021/acs.macromol.5b00744
Macromolecules 2015, 48, 4004−4011

Notes

The authors declare no competing financial interest.

■ ACKNOWLEDGMENTS

The authors thank Mr. Hsien-Tsan Lin of the Regional Instruments Center at the National Sun Yat-Sen University for his help in TEM experiments. We also thank Drs. U.-S. Jeng and C.-J. Su of the National Synchrotron Radiation Research Center (Taiwan) for their help in synchrotron SAXS experiments. The authors appreciate the Ministry of Science and Technology of the Republic of China (MOST 103-2221-E-110-081), Taiwan, for financially supporting this research.

■ REFERENCES

(1) Whitesides, G. M.; Grzybowski, B. *Science* **2002**, *295*, 2418–2421.
(2) Bates, F. S.; Fredrickson, G. H. *Annu. Rev. Phys. Chem.* **1990**, *41*, 525–557.
(3) Park, C.; Yoon, J.; Thomas, E. L. *Polymer* **2003**, *44*, 6725–6760.
(4) Mai, Y.; Eisenberg, A. Self-Assembly of Block Copolymers. *Chem. Soc. Rev.* **2012**, *41*, 5969–5985.
(5) Hsueh, H.-Y.; Yao, C.-T.; Ho, R.-M. *Chem. Soc. Rev.* **2015**, DOI: 10.1039/C4CS00424.
(6) Lee, J.-H.; Koh, C. Y.; Singer, J. P.; Jeon, S.-J.; Maldovan, M.; Stein, O.; Thomas, E. L. *Adv. Mater.* **2014**, *26*, 532–569.
(7) Fink, Y.; Urbas, A. M.; Bawendi, M. G.; Joannopoulos, J. D.; Thomas, E. L. *J. Lightwave Technol.* **1999**, *17*, 1963–196.
(8) Urbas, A. M.; Sharp, R.; Fink, Y.; Thomas, E. L.; Xenidou, M.; Fetters, L. J. *Adv. Mater.* **2000**, *12*, 812–814.
(9) Edrington, A. C.; Urbas, A. M.; DeRege, P.; Chen, C. X.; Swager, T. M.; Hadjichristidis, N.; Xenidou, M.; Fetters, L. J.; Joannopoulos, J. D.; Fink, Y.; Thomas, E. L. *Adv. Mater.* **2001**, *13*, 421–425.
(10) Deng, T.; Chen, C.; Honeker, C.; Thomas, E. L. *Polymer* **2003**, *44*, 6549–6553.
(11) Urbas, A. M.; Maldovan, M.; Derege, P.; Thomas, E. L. *Adv. Mater.* **2002**, *14*, 1850–1853.
(12) Kang, Y.; Walish, J. J.; Gorishnyy, T.; Thomas, E. L. *Nat. Mater.* **2007**, *6*, 957–960.
(13) Lee, W.; Yoon, J.; Lee, H.; Thomas, E. L. *Macromolecules* **2007**, *40*, 6021–6024.
(14) Paquet, C.; Kumacheva, E. *Mater. Today.* **2008**, *11*, 48–56.
(15) Hustad, P. D.; Marchand, G. R.; Garcia-Meitin, E. I.; Roberts, P. L.; Weinhold, J. D. *Macromolecules* **2009**, *42*, 3788–3794.
(16) Sveinbjörnsson, R. B.; Weitekamp, R. A.; Miyake, G. M.; Xia, Y.; Atwater, H. A.; Grubbs, R. H. *Proc. Natl. Acad. Sci. U.S.A.* **2012**, *109*, 14332–14336.
(17) Lee, W.; Y, J.; Thomas, E. L.; Lee, H. *Macromolecules* **2013**, *46*, 6528–6532.
(18) Kang, C.; Kim, E.; Baek, H.; Hwang, K.; Kwak, D.; Kang, Y.; Thomas, E. L. *J. Am. Chem. Soc.* **2009**, *131*, 7538–7539.
(19) Osuji, C.; Chao, C.; Bita, I.; Ober, C. K.; Thomas, E. L. *Adv. Funct. Mater.* **2002**, *12*, 753–758.
(20) Yoon, J.; Lee, W.; Thomas, E. L. *Nano Lett.* **2006**, *6*, 2211–2214.
(21) Walish, J. J.; Kang, Y. J.; Mickiewicz, R. A.; Thomas, E. L. *Adv. Mater.* **2009**, *21*, 3078–3081.
(22) Kim, E.; Kang, C.; Baek, H.; Hwang, K.; Kwak, D.; Lee, E.; Kang, Y.; Thomas, E. L. *Adv. Funct. Mater.* **2010**, *20*, 1728–1732.
(23) Ge, J.; Yin, Y. *Angew. Chem., Int. Ed.* **2011**, *50*, 1492–1522.
(24) Chan, E. P.; Walish, J. J.; Thomas, E. L.; Stafford, C. M. *Adv. Mater.* **2011**, *23*, 4702–4706.
(25) Hwang, K.; Kwak, C.; Kang, C.; Kim, D.; Ahn, Y.; Kang, Y. *Angew. Chem., Int. Ed.* **2011**, *50*, 6311–6314.
(26) Walish, J. J.; Fan, Y.; Centrone, A.; Thomas, E. L. *Macromol. Rapid Commun.* **2012**, *33*, 1504–1509.
(27) Ahn, Y.; Kim, E.; Hyon, J.; Kang, C.; Kang, Y. *Adv. Mater.* **2012**, *24*, OP127–OP130.
(28) Roe, R.-J. *Methods of X-ray and Neutron Scattering in Polymer Science*; Oxford University Press: New York, 2000; p 201.
(29) Hashimoto, T.; Fujimura, M.; Kawai, H. *Macromolecules* **1980**, *13*, 1660–1669.
(30) Hashimoto, T.; Shibayama, M.; Kawai, H. *Macromolecules* **1983**, *16*, 1093–1101.
(31) Shibayama, M.; Hashimoto, T.; Hasegawa, H.; Kawai, H. *Macromolecules* **1983**, *16*, 1427–1433.
(32) Shibayama, M.; Hashimoto, T.; Kawai, H. *Macromolecules* **1983**, *16*, 1434–1443.
(33) Mori, K.; Hasegawa, H.; Hashimoto, T. *Polymer* **1990**, *31*, 2368–2376.
(34) Balsara, N. P.; Eastman, C. E.; Foster, M. D.; Lodge, T. P.; Tirrell, M. *Makromol. Chem., Macromol. Symp.* **1991**, *45*, 213–235.
(35) Schwab, M.; Stuhn, B. *Phys. Rev. Lett.* **1996**, *76*, 924–927.
(36) Schwab, M.; Stuhn, B. *Colloid Polym. Sci.* **1997**, *275*, 341–351.
(37) Cavicchi, K.; Lodge, T. *J. Polym. Sci. Part. B Polym. Phys.* **2003**, *41*, 715–724.
(38) Maring, D.; Wiesner, U. *Macromolecules* **1997**, *30*, 660–662.

DOI: 10.1021/acs.macromol.5b00744
Macromolecules 2015, 48, 4004–4011